A structural study of PrCrO3 under extreme conditions: a comparison with the effects of doping

C. L. Bull, N. P. Funnell, C. J. Ridley

Published version information

Citation: Bull CL, Funnell NP, Ridley CJ. A structural study of $PrCrO_3$ under extreme conditions: a comparison with the effects of doping. Philos Trans A Math Phys Eng Sci. 2023 Oct 16;381(2258):20220332.

DOI: https://doi.org/10.1098/rsta.2022.0332

PHILOSOPHICAL TRANSACTIONS A

royalsocietypublishing.org/journal/rsta

Research

Article submitted to journal

Subject Areas:
High-pressure, Neutron diffraction, Functional oxides

Keywords:
Structure, distortion, polyhedral-tilting, orthochromites, lanthanide-perovskites

Author for correspondence:
Craig L. Bull
e-mail: craig.bull@stfc.ac.uk
Christopher J. Ridley
e-mail: christopher.ridley@stfc.ac.uk

A structural study of $PrCrO_3$ under extreme conditions: a comparison with the effects of doping.

C. L. Bull[1,2], N. P. Funnell[1], C. J. Ridley[1]

[1]ISIS Neutron and Muon Facility, STFC, Rutherford Appleton Laboratory, Chilton, Didcot, UK, OX11 0QX
[2]School of Chemistry, University of Edinburgh, David Brewster Road, Edinburgh EH9 3FJ, Scotland

The nuclear and magnetic structures of $PrCrO_3$ have been investigated using neutron and X–ray powder diffraction as a function of pressure and temperature. The orthorhombic symmetry (space group $Pbnm$) remains stable up to the highest temperature (1500 K) and pressure (∼6 GPa) considered. There is a crossover in the magnitude of the a and b-lattice parameters at approximately 1135 K, caused by competing effects of octahedral tilting and distortion. The material is antiferromagnetic ($T_N \approx 240$ K) with $Pb'n'm$ symmetry, with a maximum moment of 2.34(2)μ_b on the Cr^{3+} sites aligned along the direction of the a-axis. The application of pressure shows an abnormal softening in the unit-cell volume, which is suggestive of a continuous approach to a second-order phase transition. Raman spectroscopy measurements at ambient temperature were collected as a function of pressure up to ∼12 GPa, with discontinuous mode-behaviour further suggesting the existence of a transition above 7 GPa. The measured structural-changes in $PrCrO_3$ are compared extensively in the wider context of other lanthanide orthochromites, and the comparative effects of A- and B-site substitution on the polyhedral tilts and distortion are discussed.

THE ROYAL SOCIETY PUBLISHING

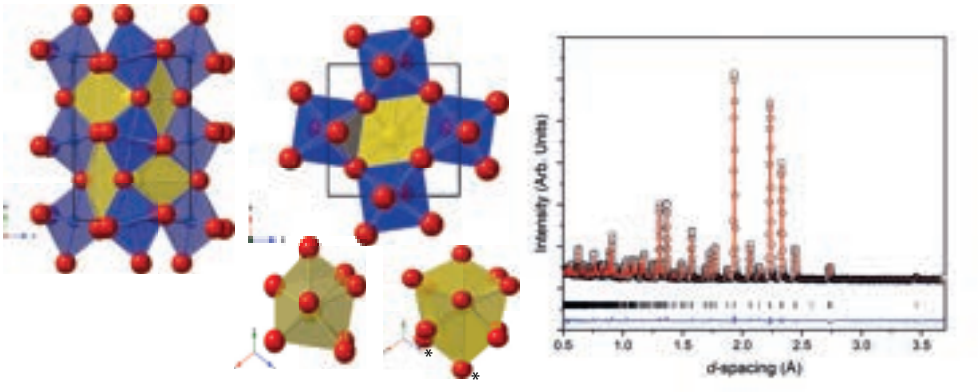

Figure 1. Left: Structure of $PrCrO_3$ under ambient conditions. The CrO_6 octahedral units are shown in blue with oxygen atoms (red) at the shared corners. The PrO_n polyhedral units are shown in yellow. The isolated PrO_n units are shown below the main structure, for n=8 (lower-left) and n=12 (lower-right). The more obvious additional oxygen atoms for n=12 are indicated by an asterisk and the remaining additional oxygen atoms are behind other more visible oxygen atoms. Right: Ambient pressure/temperature neutron diffraction pattern and Rietveld refinement of *Pbnm* structure of $PrCrO_3$. Data collected from Polaris $2\theta = 90^\circ$ detector banks. The collected data are shown as open black circles, the Rietveld fit as the red trace and the residual of the fit to the data as the blue trace. The vertical tick marks show the expected Bragg reflection positions for the orthorhombic unit cell described in the main text.

1. Introduction

As a result of chemical doping, or the variation of temperature or pressure, perovskite-like materials (with general chemical formula ABX_3) can adopt a wide range of different structural distortions away from the aristotype cubic structure (parent cell). The structure may be altered via three routes; a) distortion of the BO_6 octahedra (for example, a Jahn-Teller distortion), b) a tilt (or rotation) of the rigid BX_6 octahedral units around the principal axes of the parent cell [1] and c) A-site cation displacements [2].

These distortion mechanisms drive many of the resultant electronic, magnetic, and other physical properties of these materials, and have been studied extensively in the literature; a full review of which is beyond the scope of this study. Here, we present a structural study of $PrCrO_3$, one of a series of orthorhombic perovskites (with the general formula $RCrO_3$ where R= rare earth) which show complex magnetic behaviour at low temperature and interesting magnetoelectric and multiferroic properties [3]. The structural distortions of these materials can be driven further towards higher/lower symmetry structures using extreme conditions, such as high pressures and temperatures. This can be understood using Landau theory, while the relative raising or lowering of symmetry can be predicted using qualitative methods [4].

The semiconducting orthorhombic $PrCrO_3$ (with Cr in the +3 oxidation state) has been shown by optical methods to have an estimated band gap in the range of 3.20–3.26 eV and as a result is a good candidate for opto-electronic devices [5]. Magnetically, the material is antiferomagnetic with a Néel temperature of 237 K. At 4.2 K the Cr^{3+} spin structure is G-type with an additional weak ferromagnetic component laying along the c-axis [6]. Permittivity and impedance spectroscopic measurements suggest that the material may be relaxor ferroelectric-like in nature [7]. Very few structural studies have been performed on the material to date [3,8]. We have studied the structural behaviour of $PrCrO_3$ using a combination of neutron and X-ray diffraction, both as a function of pressure and temperature. We have also investigated the behaviour of the Raman active modes where for some vibrational modes softening is found to occur across the pressure range studied.

2. Experimental

Sample Synthesis

$PrCrO_3$ was prepared by mixing stoichiometric quantities of dried Pr_6O_{11} and Cr_2O_3 (Sigma–Aldrich >99%) [3]. The ground powder was pelletised prior to annealing at 923 K for 12 hours in a Pt crucible. The annealed pellet was reground and re-pelletised and annealed for a further 24 hours at 1223 K and this process repeated at 1623 K [3]. The sample was then characterised by X–ray diffraction using a Bruker D2 diffractometer to confirm phase purity.

Ambient–Pressure Diffraction

The ambient pressure, ambient temperature structure was confirmed using the Polaris instrument at the ISIS Neutron and Muon Source, UK [9]. Low-temperature neutron powder diffraction data were collected using the GEM instrument at the ISIS Neutron and Muon Source [10]. Approximately 2 g of $PrCrO_3$ was dried under vacuum at 390 K before being loaded into a 6 mm vanadium canister in an inert atmosphere, sealed using indium. The sample was cooled to 10 K, allowed to reach equilibrium for 15 min, and data were collected on warming the sample in 10 K steps up to 100 K, and 20 K steps from 100-280 K. The sample was allowed 5 min to reach equilibrium at each temperature, before starting the measurement. Each temperature-point was measured for approximately 1 hr. High-temperature powder X–ray diffraction (PXRD) measurements were collected using a Rigaku Smartlab with a Cu Kα monochromator. The sample was loaded into a 0.8 mm deep alumina sample holder, and mounted onto the high-temperature stage. Data were collected over the range $20^o < 2\theta < 65^o$ for approximately 1 hr per measurement. The sample was heated in 100 K steps, with data collected on heating, allowing for 15 min to reach equilibrium at each point. Symmetry-adapted basis vector decomposition was performed using ISODISTORT [11], the resultant modes can be visualised using the associated ISOVIZ program. Representative parent and distorted cif structure files, and the resultant ISOVIZ visualisation file, are included as part of the Supplementary Information (SI).

High–Pressure Neutron Powder Diffraction

High–pressure neutron powder diffraction measurements were performed on the PEARL instrument at the ISIS Neutron and Muon Source, UK [12]. Powdered $PrCrO_3$ was loaded into an null-scattering TiZr gasket. Pb was included as a pressure-marker, and perdeuterated methanol:ethanol (4:1 by volume) was used as a pressure medium. The gasket was loaded using single-toroid ZrO_2/Al_2O_3 anvils within a V3 Paris–Edinburgh (PE) press [13]. Diffraction patterns were measured in the fixed $2\theta = 90^o$ scattering geometry, for approximately 2 hours per pressure point. The raw data were corrected for detector efficiency and anvil attenuation using the Mantid software [14]. Rietveld refinement was performed using the GSAS suite of programs [15]. The bulk modulus and axial compressibilties were determined using the PASCal program [16].

High–Pressure Raman Spectroscopy

High-pressure Raman measurements were performed using a Merrill-Basset diamond anvil cell [17]. A stainless steel gasket was preindented from an initial thickness of 200 μm to 75 μm, and drilled with a sample hole of 250 μm diameter. A small ruby sphere was used as pressure marker, determined by ruby fluorescence measurements [18]. Methanol:ethanol (4:1 by volume) was used as a pressure transmitting medium. Raman spectra were collected using an in-house Raman system equipped with a Princeton Instruments SP2500i spectrometer using a 1800 g holographic blaze grating. A diode laser (λ = 532.23 nm) was focused using a 20$\times$ Mitutoyu objective lens.

3. Results and Discussion

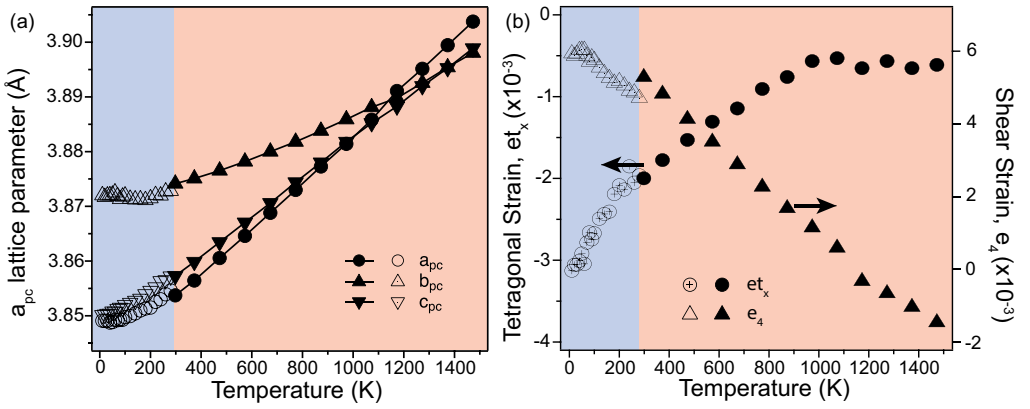

Figure 2. (a) Temperature dependence of the lattice parameters of $PrCrO_3$ reduced to their pseudo-cubic form (see main text). (b) Calculated tetragonal (et_x) and shear (e_4) strain of the system as a function of temperature (the arrows indicate which data set is plotted on each axis). In both figures, the data below 280 K (blue region) were collected from neutron powder diffraction (open symbols), and those above (red region) were collected using X-ray diffraction (solid symbols).

Ambient–Pressure Crystallographic Structure

Figure 1 shows the neutron diffraction pattern (and Rietveld refinement) for powdered $PrCrO_3$ collected under ambient conditions using the Polaris instrument. The derived structural parameters from the Rietveld fit are given in Table 1. The orthorhombic ($Pbnm$) structure is that of a distorted perovskite, Glazer tilt $a^-a^-c^+$, where the CrO_6 octahedra are tilted away from the ideal cubic structure via the R4+ and M3+ primary distortion modes ($Pm\bar{3}m$ parent with B-site at the origin, [**a**+**b**, **b**-**a**, 2**c**]; $(\frac{1}{2},\frac{1}{2},0)$) [1,19]. A schematic of these distortion modes is available in the SI. Although tilted, the CrO_6 octahedra are regular with the Cr–O distances ranging from 1.972–1.982 Å with a weighted average value of 1.976 Å, see Figure 1. The Pr–O–Pr bond angles along the chains of the CrO_6 octahedra are 155°, and the resultant tilts are calculated to be 8.82° for the anti-phase a^- (R4+ mode), and 8.73° for the in-phase c^+ (M3+ mode) at ambient conditions.

There is some ambiguity in the literature over the coordination value of the A-site cation in these materials. In $PrCrO_3$, the PrO_n polyhedra are distorted with Pr–O distances ranging from 2.389–2.729 Å if $n = 8$ is assumed, with a maximum Pr–O distance of 3.218(4) Å if $n = 12$. The structural differences in these two different polyhedra are shown in Figure 1. For the PrO_{12} unit, the bond lengths are significantly longer than is accepted for a typical Pr–O bond, and the resultant polyhedral shape is highly irregular within 8 and 12 fold coordinated PrO_n polyhedra the average values are 2.478 Å and 2.672 Å respectively [20]. It is therefore more physical in this case to assume $n = 8$ coordination. We list some values for both cases, in order to aid comparison with the literature.

$PrCrO_3$ remains orthorhombic down to the lowest temperature measured, 10 K. The mean volumetric thermal-expansion coefficient was determined to be $\bar{\alpha}_v = 22.4 \times 10^{-6}\,\mathrm{K}^{-1}$ (calculated over the full temperature range 10-1473 K), comparable to the other orthochromites [21,22]. The system becomes antiferromagnetic below $T_N \approx 240$ K (see SI), with the appearance of a strong magnetic reflection at 4.46 Å . The $Pb'n'm$ model was fitted against teh data, Γ_3 irreducible representation, with a maximum refined moment of 2.34(2)μ_b on the Cr^{3+} sites at 10 K along the a-axis. The data were insufficient to fit any moment on Pr^{3+} site, or any canting of the moment on the Cr site, both resulting in divergence of the refinement. Both the CrO_6 octahedra, and the PrO_8 polyhedra reduce in volume at a comparable rate, with extremely small changes in the tilt (the M3+ mode is invariant, while the R4+ anti-phase tilt increases slightly to 8.95°) at 10 K. Looking

more closely at the octahedral distortion on heating, the R5+ (Cr) mode increases in magnitude by ∼25%, while the X5+ (Cr) mode decreases by only ∼1%, the X5+ (Pr) mode reduces by ∼7%. This leads to an overall reduction in the distortion of the Pr-polyhedra, at the expense of some distortion of the Cr-octahedra.

Table 1. Refined structural parameters, and resulting bond lengths, for $PrCrO_3$ from neutron powder diffraction at 10 K (GEM), and 300 K (Polaris). The symmetry is $Pbnm$ with Pr and O1 sitting on the *4c* $(x, y, \frac{1}{4})$, Cr sitting on the *4b* $(\frac{1}{2}, 0, 0)$, and O2 on the *8d* (x, y, z) Wyckoff sites respectively. The bond lengths for Pr are shown assuming 8-fold coordination to O, with 2x distinct Pr-O1 bonds, and 3x distinct Pr-O2 bonds. The additional bond lengths assuming 12-fold coordination to O are shown below in [square brackets].

Temperature (K)	10	300
a-axis length (Å)	5.4435(3)	5.45346(6)
b-axis length (Å)	5.4759(4)	5.47864(7)
c-axis length (Å)	7.7003(4)	7.71796(8)
Unit-cell volume (Å^3)	229.53(2)	230.593(5)
Pr x, y	-0.0093(8), 0.0369(4)	-0.0065(3), 0.03591(13)
O(1) x, y	0.0772(5), 0.4849(4)	0.07546(17), 0.48450(13)
O(2) x, y, z	-0.2890(3), 0.2879(3), 0.0403(2)	-0.28747(9), 0.28798(10), 0.03960(7)
wRp, Rp, χ^2	4.72 % 4.03 %, 1.37	2.4 % 3.6 %, 3.04
Cr, μ_x (μ_B)	2.339(16)	0
Cr–O(1) (Å)	1.9721(6)	1.9727(9)
Cr–O(2) (Å)	1.9751(16), 1.9799(16)	1.972(3), 1.982(2)
Pr–O(1) (Å)	2.369(5), 2.298(3)	2.389(7), 2.507(4)
	[3.059(3), 3.104(5)]	[3.046(4), 3.088(7)]
Pr–O(2) (Å)	2.382(3), 2.610(3), 2.712(3)	2.389(7), 2.603(4), 2.729(4)
	[3.286(3)]	[3.281(4)]

The symmetry remains orthorhombic up to the maximum temperature considered, 1500 K. Cooperative changes within the material at the atomic scale, results in lattice strains (e) on a macroscopic scale, which are the driving forces for a transition [23]. The spontaneous strains are calculated as $(x_{pc} - a_0)/a_0$, where x_{pc} are the pseudo–cubic lattice parameters calculated in the orthorhombic phase (a_{pc}, b_{pc}, c_{pc}), and a_0 is in this case an isotropically strained lattice parameter that would occur at the same pressure in the high symmetry, cubic phase. Since there is no experimentally observed cubic phase of $PrCrO_3$ from which a_0 can be extrapolated, the expected cubic behaviour is instead estimated from the pseudo–cubic unit–cell volume (V_{pc}) using $a_0 \approx \sqrt[3]{V_{pc}}$. Figure 2 shows the variation in spontaneous strain e_{tx}, and shear strain e_4, with temperature. There is a crossover in the lattice parameters from $(b > a) \rightarrow (a > b)$ at 1135 K, which corresponds to a point where the tetragonal strain plateaus, and the shear strain crosses zero. On continued heating, the tetragonal strain remains unchanged, while the modulus of the shear strain begins to increase again. This phenomenon isn't unusual in orthorhombic perovskites; while the cross-over is usually induced through changes in chemical composition, it is well documented as a temperature effect in $LaFeO_3$ [24,25]. The origins of this cross-over are the competition between the octahedral tilting, and octahedral distortion. The octahedral rotation may encourage the lengthening of one axis relative to the other, which is then either accommodated or resisted by the in-plane distortion of the octahedra. Since the PXRD data are dominated by scattering from the Pr and Cr, it was not possible to accurately refine the O-positions to investigate the balance between these two effects in $PrCrO_3$.

To compare the high-temperature behaviour with other $ACrO_3$ (A= lanthanide) compounds, a similar degree of thermal expansion is observed for A=Nd, with no change in symmetry, and no cross-over in the a- and b-lattice parameters [22]. For A=La, the compound undergoes a phase transition from orthorhombic to rhombohedral symmetry at approximately 550 K, resulting

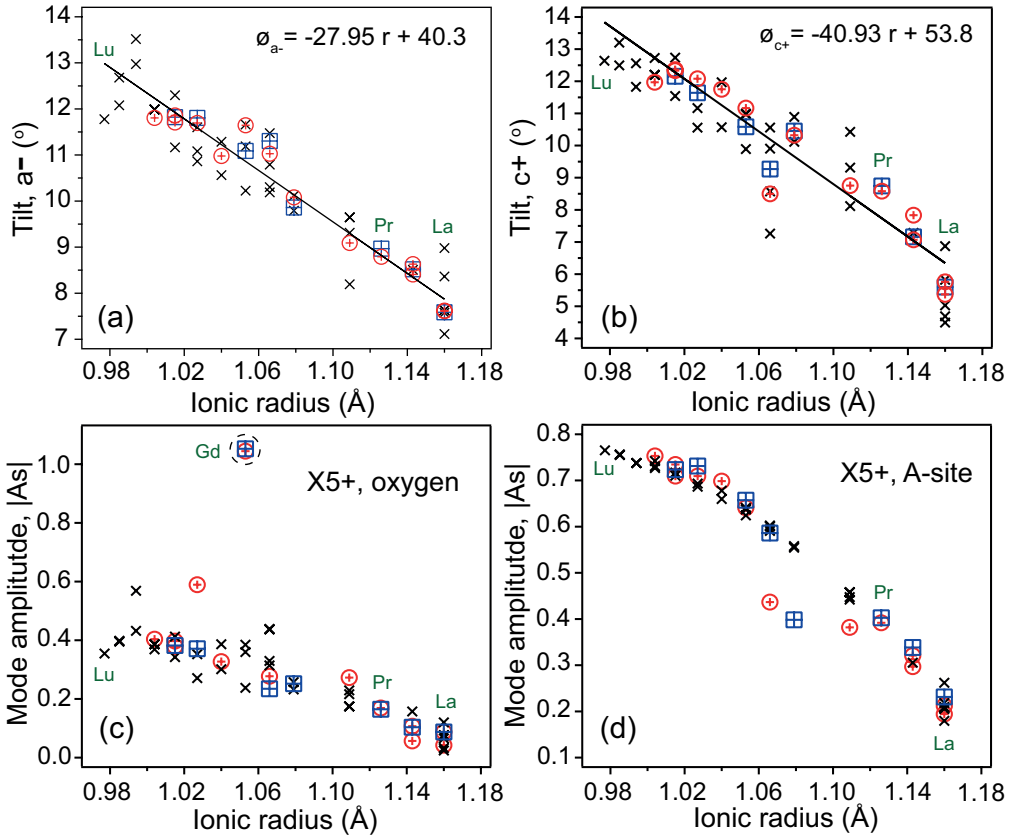

Figure 3. Calculated anti-phase, a^- (a), and in-phase, c^+ (b), tilt angles plotted as a function of A-site ionic radius for a number of lanthanide orthochromites found in the literature [22,26–49], and from the present study. The ionic radii are compared assuming 3+ oxidation, and 8-fold coordination [50]. The lines in both (a) and (b) are linear best fits to the neutron data at ambient temperature. Also shown are the calculated distortion mode amplitudes for X5+, oxygen octahedra (c) A-site cation (d). The outlier in (c) is for the Gd compound, so it is assumed that absorption corrections have led to an inaccurate structure determination from the neutron data. In all figures, the crosses (×) are calculated from X-ray diffraction data (room temperature), while the squares (⊞, low temperature 2-20 K) and circles (⊕, room temperature) are calculated from neutron diffraction data.

in a discrete drop in the CrO_6 polyhedral volume (approximately 0.7%) [51]. On continued heating, the volumetric thermal expansion of $LaCrO_3$ is comparable to $PrCrO_3$. The very small change in tilt angle with changing temperature is typical of the lanthanide orthochromites. To demonstrate this, a large number of reported orthochromite structures from the literature have been compared as a function of A-site ionic radius and temperature [22,26–49]. The tilts were calculated consistently through symmetry-adapted basis vector decomposition [11,19,52] allowing for a proper distinction between octahedral tilt, and distortion. This information is summarised in Figure 3. While neutron data are more sensitive to oxygen information, a number of structures reported from X-ray measurements are also included in the comparison. It is clear from comparing the high- and low- temperature values determined from neutron diffraction that the tilt angles and polyhedral distortions are relatively insensitive to temperature changes (2-300 K) in all lanthanide orthochromites. Instead, the size of the A-site cation dominates the tilt of the oxygen octahedra, varying by 5-6° over the series. In all cases the reduction in A-site cation size results in increased levels of tilt, and distortion of both the oxygen octahedra, and the A-site polyhedral units, as evidenced by the increase in the X5+ distortion modes. The R5+ (O) and M2+

(O) modes, not shown in the figure, are approximately invariant and close to zero in amplitude. The R5+ (A-site) mode shows a similar increase in amplitude with reduction in cation radius. In contrast, B-site cation size has the opposite influence on the tilts in the series $LaBO_3$ (B=Sc, Ti, V, Cr, Mn, Fe, Co, Ni, Cu). There is an approximately linear decrease in the tilts with reduction in B-site cation radius from Sc to Fe [25,53–57], and an eventual raising of symmetry to rhombohedral for the Co - Cu compounds.

High–Pressure Structural Behaviour

Figure 4 shows the neutron powder diffraction pattern and associated Rietveld refinement fit to $PrCrO_3$ at 0.01 GPa. The derived structural parameters are in close agreement with those determined at ambient pressure. Upon compression to 5.6 GPa no change in crystal symmetry is observed, only a decrease in all unit–cell parameters, see Figure 5. The pseudo–cubic lattice parameter a_{pc} (parallel to the long Pr–O bonds in the AO_6 polyhedral unit) is more compressible (2.72 TPa^{-1}) than both b_{pc} (0.18 TPa^{-1}) and c_{pc} (0.92 TPa^{-1}). These values are similar to the anisotropic compressibility reported for $HoCrO_3$ [58], and similarly for $GdCrO_3$, $EuCrO_3$ and $SmCrO_3$ [59], and $YCrO_3$ [60]. However, while the *a*-axis (in the $Pbnm$ setting) for $NdCrO_3$ was also found to be significantly more compressible than the other axes, the *b*-axis expanded slightly under pressure [22]. This discrepancy observed in $NdCrO_3$ may be linked to some non-hydrostatic components in the applied pressure, evidenced by the presence of peak broadening in the diffraction data [22].

The unit–cell volume variation with pressure is shown in Figure 5, and demonstrates a clear negative curvature, which could not be accounted for using a 2^{nd}-order Birch–Murnaghan equation–of–state. Fitting instead to the 3^{rd}-order, the derived values for the bulk modulus (B_0) and first pressure-derivative (B') are 258(3) GPa and -13.89(7) respectively. The value of V_0 of 230.12(3) $Å^3$ is very close to that extracted from refinement of ambient pressure diffraction data (see Table 1). The value of B_0 is significantly different to that calculated from density functional theory [61], though in good agreement with the experimental trend of values from other rare-earth orthochromites [22,58–60,62]. The negative curvature (B') of the volume–pressure curve is not seen in the other rare-earth orthochromites, suggesting that the material abnormally softens with pressure. This has, however, been observed in other oxides and perovskites and may be associated with the material exhibiting the onset of ferroelastic properties [63]; similar behaviour has been seen in ZrO_2 and $BaTiO_3$ [64–66]. One explanation is that softening of the material can be a prelude to a phase transition, however, for $PrCrO_3$ the softening is observed throughout the pressure range studied. A second explanation may be that there are anomalies in the higher-order elastic constants (presenting as large pressure gradients in shear wave velocities with negative curvature). Such anomalous behaviour may well be a result of "soft-mode" behaviour, often observed in high-symmetry phases near the critical pressure of a second-order phase transition [67].

Figure 5 shows the variation in spontaneous strain e_{tx}, and shear strain e_4, with increasing pressure. This shows that the tetragonal-strain reduces, towards the cubic form (which necessitates, $e_{tx} = 0$) albeit with some non-linear behaviour. At approximately 1.2 GPa, the strain crosses zero, and continues to increase linearly. The *ab*-shear strain, e4, increases continuously with applied pressure. A simple interpretation of this is that the pseudo-cubic cell changes from being tetragonally compressed to elongated along the orthorhombic *c*-axis, while the increased level of *ab*-shear retains the orthorhombic symmetry through the cross-over point.

To better understand how the orthorhombic symmetry is maintained, changes in the tilt and distortion of the polyhedral units should also be considered. The three distinct Cr–O bond lengths within the CrO_6 octahedra tend to decrease with pressure, with the average of the three (<Cr–O>) reflecting this behaviour with an approximately linear decrease, see Figure 6. The average Pr–O bond in the PrO_8 polyhedra (<Pr–O>) is less compressible than <Cr–O>, which is also apparent in the polyhedral volume changes also shown in Figure 6. The Baur geometric distortion indices of both polyhedra are approximately invariant with increasing pressure [68]. The relative

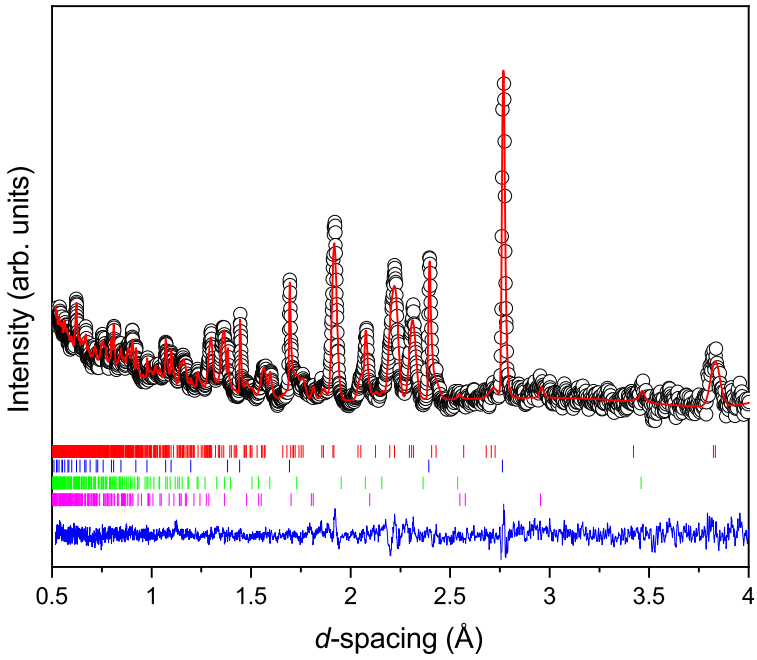

Figure 4. Neutron diffraction pattern and Rietveld refined fit of $PrCrO_3$ at 5.6 GPa. The experimental data is shown as open circles, the Rietveld fit as the red line and the blue line is the residual of the fit to the data. The tick marks show the expected positions of reflections from orthorhombic $PrCrO_3$ (red), Pb pressure marker (blue), Al_2O_3 (green) and ZrO_2 (purple), from top to bottom respectively. The Al_2O_3 and ZrO_2 contribution are from the anvil material used in the high-pressure assembly.

compressibility of the two polyhedra is consistent with the predictions based on the bond valence sum (BVS) ratio, as detailed in the literature [4,69,70]. Based on the ambient pressure structure, the ratio of BVS for the PrO_8 and CrO_6 polyhedra is 1.31, which implies that the CrO_6 octahedra should be more compressible than the PrO_8 polyhedra, and that the overall structure would be expected to become more symmetric with increasing pressure, consistent with other formally $3^+/3^+$ (A-site/B-site) charged perovskite systems. The octahedral units show a reduction in tilt angle, with a^- reducing from approximately $8.85^\circ \rightarrow 8.5^\circ$, and c^+ from $8.6^\circ \rightarrow 8.3^\circ$, though still considerably tilted away from the undistorted cubic sub-cell. Additionally, there is a linear increase in the X5+ (Pr) mode by approximately 20% at 5.5 GPa, suggesting that the application of pressure has a similar affect on the distortion of the Pr-O polyhedra as reducing the temperature. The R5+ (O) mode also increases approximately linearly with pressure, related to the *ac*-plane distortion of the CrO_6 octahedra.

There are very few high-pressure structural studies on the lanthanide orthochromites in the literature, with the majority of them being X-ray diffraction studies, only reporting the changes in lattice parameters [22,58–60]. A neutron study of $LaCrO_3$ showed that it was found to change from orthorhombic to rhombohedral symmetry at approximately 5 GPa [62,71,72]. Analysis of the symmetry-adapted basis vectors from the work of Zhou et al. [62] show that the changes in tilt are similarly small to those in $PrCrO_3$ over a similar pressure range. However, unlike the changes observed in $PrCrO_3$, the a^- tilt decreases from $7.76^\circ \rightarrow 7.59^\circ$, while the c^+ tilt increases from $4.82^\circ \rightarrow 5.27^\circ$. The X5+ (La) and R5+ (La) modes both decrease in amplitude, showing a

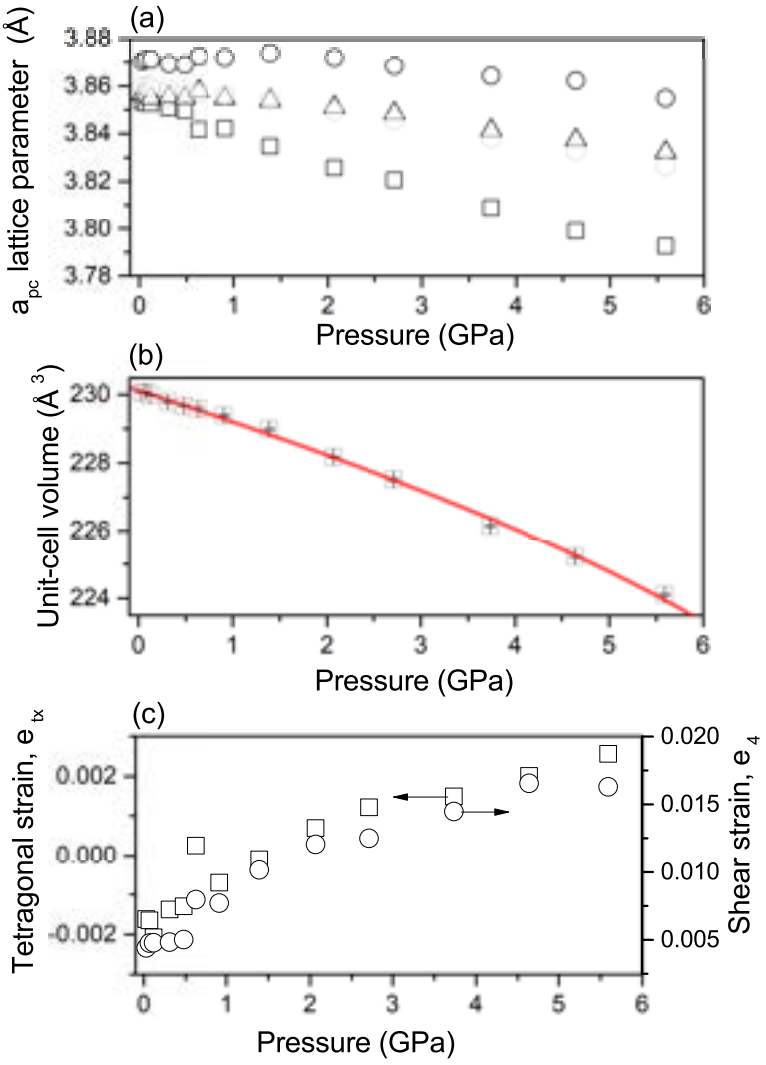

Figure 5. Behaviour of unit-cell parameters of $PrCrO_3$ with pressure at 290 K. (a) Variation in pseudo-cubic lattice parameter where $a_{pc}=a_o/\sqrt{2}$ (open squares), $b_{pc}=b_o/\sqrt{2}$ (open circles) and $c_{pc}=c_o/2$ (open triangles). The transparent hexagon symbols are the pseudo–cubic lattice parameter (a_{pc}) determined from the orthorhombic unit cell volume (V_o) as $a_{pc}=\left(\frac{V_o}{4}\right)^{1/3}$. (b) Change in unit–cell volume (squares) with pressure. The 3^{rd} order Birch–Murnaghan EoS fit to the data is shown as solid red line and determined values given in main text. Error bars are shown but smaller than symbols. (c) Determined tetragonal strain (e_{tz}) and shear strain (e_4) with pressure (see text for details).

reduction in La–O polyhedral distortion, while M2+ (O) increases linearly with amplitude. This mode is related to the *ab*-plane distortion of the CrO_6 octahedra, and isn't seen to increase with increasing pressure in $PrCrO_3$, while the R5+ (O) mode is unchanged with pressure in $LaCrO_3$. The reason for these differences is linked to the larger A-site ionic radius for La, which results in a less tilted, but more distorted polyhedral system at ambient pressure (see Figure 3).

The previous study of $NdCrO_3$ with pressure only reports changes in lattice parameters with pressure, though the structure reportedly remains orthorhombic up to the maximum 6.4 GPa considered, and the volumetric compression shows no clear softening [22]. $LuCrO_3$, $TbCrO_3$, $GdCrO_3$, $EuCrO_3$ and $SmCrO_3$ were investigated up to approximately 20 GPa with X-ray

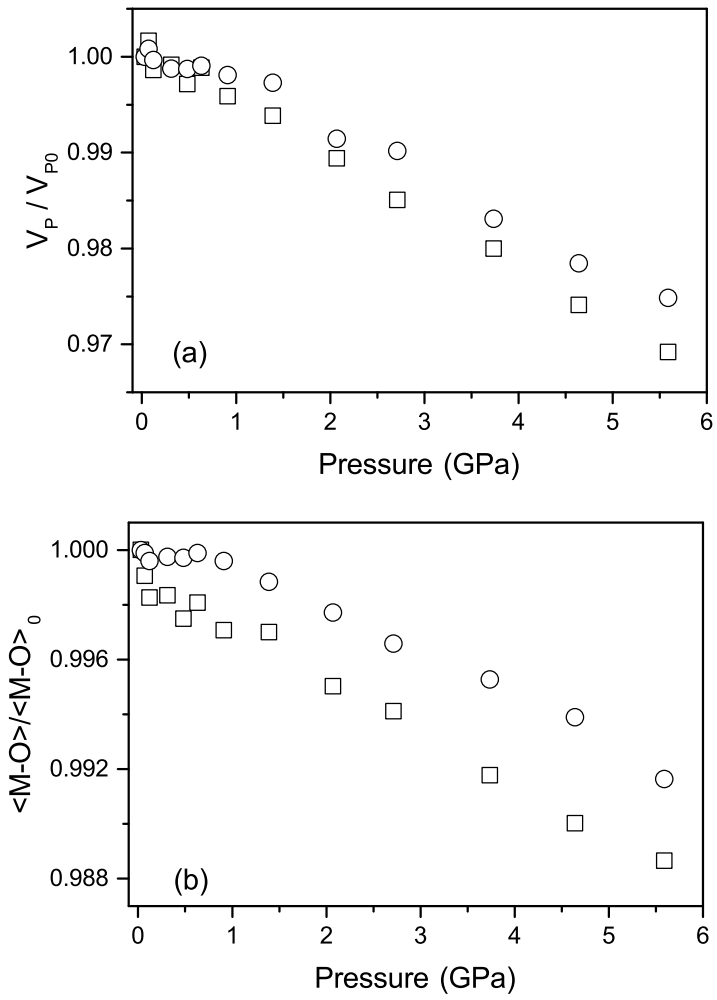

Figure 6. (a) Variation in the CrO_6 (□) and PrO_8 (◯) polyhedral volumes with pressure in $PrCrO_3$. (b) Variation in the average M–O bond length ($< M - O >$) within the CrO_6 (□) and PrO_8 (◯) polyhedra. The values in both (a) and (b) are normalised against ambient pressure values.

diffraction [59]. The authors concluded that larger A-site cation radii lead to the stabilisation of a less distorted high-pressure structure (as with $LaCrO_3$), whereas smaller A-site cations instead accommodate more highly distorted A-site polyhedra, retaining orthorhombic symmetry [59]. This finding seems consistent with what is observed with $YCrO_3$ up to 60 GPa [60]. The bulk modulus determined in the present study, is consistent with those determined for the other orthochromites, which shows an approximate trend of a reduction in B_0 with increases A-site cation radius.

High–Pressure Raman Spectroscopy

Figure 7 shows the ambient pressure Raman spectra of $PrCrO_3$. Symmetry allows 24 Raman active modes ($7A_g + 5B_{1g} + 7B_{2g} + 5B_{3g}$) [73]. There are 16 discernible Raman modes in the

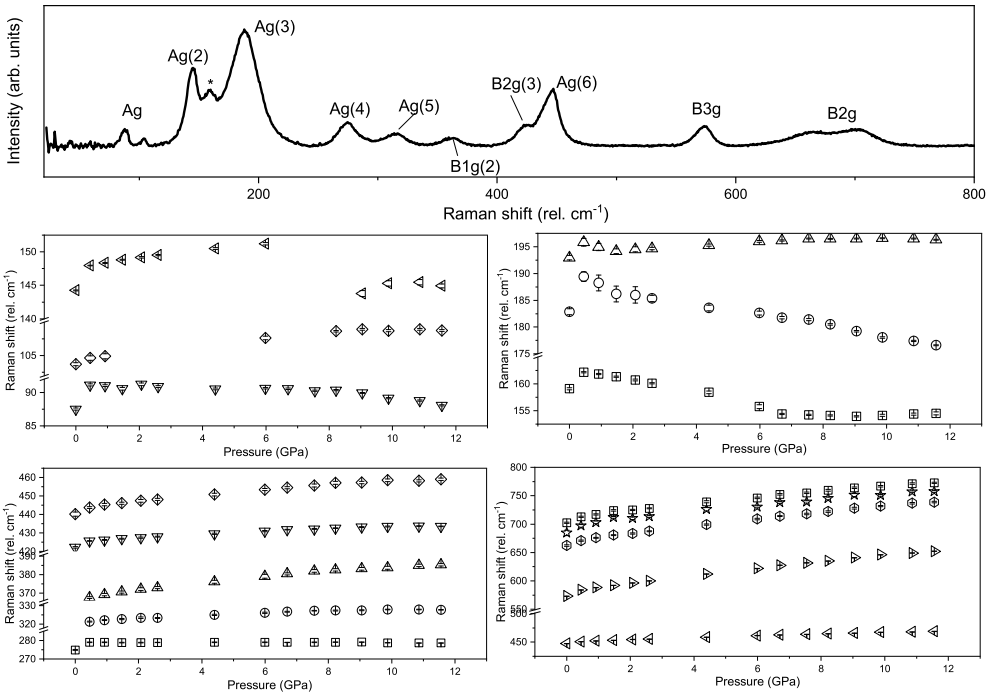

Figure 7. Raman spectra of $PrCrO_3$ at ambient conditions, with mode assignments (top). Behaviour of Raman modes of $PrCrO_3$ with increasing pressure (bottom). Note that there are breaks in the y-axes of all of the plots.

spectral region measured, the positions of which are in close agreement with those assigned in previous studies (the assignments are labelled in Figure 7). Interestingly, we also observe a mode at $ca.$ 160 cm^{-1} which in previous studies could not be assigned, suggested to be a result of an impurity however, no such impurity is observed in the neutron diffraction data [73]. The modes above 600 cm^{-1} do not correspond to normal Raman modes expected of the $Pbnm$ orthorhombic structure. However, these may be ascribed to some form of local lattice imperfection and could be formed by distorted $Cr^{4+}O_6$ and/or $Cr^{4+}O_n$ (n≠6) [74]. Similarly, this is suggested to occur in $LaCrO_3$ which is thought to be cation-deficient $La_{1-y}CrO_3$ and $LaCr_{1-x}A_xO_3$ (A=Co,Ni) [74]. In the octahedral structure, Cr^{4+} has partially filled t_{2g} orbitals in which a Jahn-Teller distortion affecting the local environment of the Cr^{4+} may be present [74]. Given that the unassigned mode at $ca.$ 160 cm^{-1} is observed to a similar extent in the previously reported studies, it may be a result of local symmetry breaking, rather than chemical impurity [73].

The majority of the observed modes shift to higher energy with increasing pressure (see Figure 7). However, in particular the B_{2g} and A_g modes are found to soften and are related to rotational modes and some small discontinuous behaviour is observed in these and other modes around 7 GPa. Such behaviour may be indicative of a phase transition, at pressures beyond that considered in the diffraction study.

4. Conclusion

Neutron and X–ray diffraction has been used to fully characterise the structure of $PrCrO_3$ as a function of pressure and temperature. The variable temperature data show that the sample remains orthorhombic over the full temperature range considered (10-1500 K), with a crossover in the magnitude of the *a*- and *b*-lattice parameters at approximately 1135 K, driven by competition between the tilt and distortion of the oxygen octahedra. In both the temperature and pressure

studies, the changes in the octahedral tilts were found to be small, not changing by more than $\sim 0.1^\circ$ and $\sim 0.3^\circ$ respectively, while the relative unit-cell strains changed more substantially. In comparison with other lanthanide orthochromites, the induced structural changes are relatively small, suggesting that A- or B-site doping can induce significantly larger effects than the temperatures or pressures considered in this study.

The high-pressure data collected at ambient temperature show an unusual softening in the unit-cell volume, which we suggest may be a prelude to a second-order phase transition at higher-pressures still, which may also be apparent in the high-pressure Raman spectra at *ca.* 7 GPa. As both La and Pr have relatively large ionic-radii (within the lanthanide series), it is expected that this transition would be similar in nature to that observed in $LaCrO_3$ [62]. Whether a similar trend exists across the series remains unknown, though a future study with a more highly-distorted ambient structure would be interesting for comparison. With this in mind, it seems likely that the Néel temperature of $PrCrO_3$ will shift to higher temperatures with applied pressure, though further experimental data are required to verify this [75].

Acknowledgements. The authors would like to thank Daniel Nye (Materials Characterisation Lab, ISIS Neutron and Muon Source) for his assistance with the high temperature X-ray diffraction measurements, and the Science and Technology Facilities Council (STFC) for access to the PEARL, GEM, and Polaris instruments at the ISIS Neutron and Muon Source. Particular thanks to the instrument scientists, Ron I. Smith (Polaris) and Ivan da Silva (GEM) for their assistance with the ambient-pressure measurements, and to the ISIS Neutron and Muon Source Cryogenics section for preparing the cryostat for the low-temperature measurements. Data supporting this study are openly available in the Supplementary Information (SI) and from the STFC DataGateway at the DOIs referenced here [76–78].

References

1. Glazer AM. 1972 The classification of tilted octahedra in perovskites. *Acta Crystallographica Section B* **28**, 3384–3392. (10.1107/S0567740872007976)
2. Woodward PM. 1997 Octahedral Tilting in Perovskites. I. Geometrical Considerations. *Acta Crystallographica Section B* **53**, 32–43. (10.1107/S0108768196010713)
3. Kumar S, Coondoo I, Vasundhara M, Kumar S, Kholkin AL, Panwar N. 2017 Structural, magnetic, magnetocaloric and specific heat investigations on Mn doped $PrCrO_3$ orthochromites. *Journal of Physics: Condensed Matter* **29**, 195802. (10.1088/1361-648x/aa666c)
4. Zhao J, Ross NL, Angel RJ. 2004 New view of the high-pressure behaviour of $GdFeO_3$-type perovskites. *Acta Crystallographica Section B* **60**, 263–271. (10.1107/S0108768104004276)
5. Mguedla R, Ben Jazia Kharrat A, Taktak O, Souissi H, Kammoun S, Khirouni K, Boujelben W. 2020 Experimental and theoretical investigations on optical properties of multiferroic $PrCrO_3$ ortho-chromite compound. *Optical Materials* **101**, 109742. (https://doi.org/10.1016/j.optmat.2020.109742)
6. Gordon JD, Hornreich RM, Shtrikman S, Wanklyn BM. 1976 Magnetization studies in the rare-earth orthochromites. V. $TbCrO_3$ and $PrCrO_3$. *Physical Review B* **13**, 3012–3017. (10.1103/PhysRevB.13.3012)
7. Prasad BV, Rao GN, Chen J, Babu DS. 2011 Relaxor ferroelectric like giant permittivity in $PrCrO_3$ semiconductor ceramics. *Materials Chemistry and Physics* **126**, 918–921. (https://doi.org/10.1016/j.matchemphys.2010.12.013)
8. Mguedla R, Ben Jazia Kharrat A, Saadi M, Khirouni K, Chniba-Boudjada N, Boujelben W. 2020 Structural, electrical, dielectric and optical properties of $PrCrO_3$ ortho-chromite. *Journal of Alloys and Compounds* **812**, 152130. (https://doi.org/10.1016/j.jallcom.2019.152130)
9. Smith RI, Hull S, Tucker MG, Playford HY, McPhail DJ, Waller SP, Norberg ST. 2019 The upgraded Polaris powder diffractometer at the ISIS neutron source. *Review of Scientific Instruments* **90**.
10. Hannon AC. 2005 Results on disordered materials from the GEneral Materials diffractometer, GEM, at ISIS. *Nuclear Instruments and Methods in Physics Research Section A: Accelerators, Spectrometers, Detectors and Associated Equipment* **551**, 88–107. Proceedings of the E-MRS Fall Meeting 2004, Symposium D.

11. Stokes HT, Hatch DM, Campbell BJ, Tanner DE. 2006 ISODISPLACE: a web-based tool for exploring structural distortions. *Journal of Applied Crystallography* **39**, 607–614.
12. Bull CL, Funnell NP, Tucker MG, Hull S, Francis DJ, Marshall WG. 2016 PEARL: the high pressure neutron powder diffractometer at ISIS. *High Pressure Research* **36**, 493–511. (10.1080/08957959.2016.1214730)
13. Besson JM, Nelmes RJ, Hamel G, Loveday JS, Weill G, Hull S. 1992 Neutron powder diffraction above 10 GPa. *Physica B* **180**, 907–910.
14. Arnold O, Bilheux JC, Borreguero JM, Buts A, Campbell SI, Chapon L, Doucet M, Draper N, Ferraz Leal R, Gigg MA, Lynch VE, Markvardsen A, Mikkelson DJ, Mikkelson RL, Miller R, Palmen K, Parker P, Passos G, Perring TG, Peterson PF, Ren S, Reuter MA, Savici AT, Taylor JW, Taylor RJ, Tolchenov R, Zhou W, Zikovsky J. 2014 Mantid Data analysis and visualization package for neutron scattering and μSR experiments. *Nuclear Instrumentation Methods A* **764**, 156–166. (http://dx.doi.org/10.1016/j.nima.2014.07.029)
15. Toby BH. 2001 *EXPGUI*, a graphical user interface for *GSAS*. *Journal of Applied Crystallography* **34**, 210–213. (10.1107/S0021889801002242)
16. Cliffe MJ, Goodwin AL. 2012 *PASCal*: a principal axis strain calculator for thermal expansion and compressibility determination. *Journal of Applied Crystallography* **45**, 1321–1329.
17. Merrill L, Bassett WA. 1974 Miniature diamond anvil pressure cell for single crystal X-ray diffraction studies. *Review of Scientific Instruments* **45**, 290.
18. Syassen K. 2008 Ruby under pressure. *High Pressure Research* **28**, 75.
19. Knight KS. 2009 Parameterization of the crystal structures of centrosymmetric zone-boundary-tilted perovskites: an analysis in terms of symmetry-adapted basis-vectors of the cubic aristotype phase. *The Canadian Mineralogist* **47**, 381–400.
20. Gagné OC. 2018 Bond-length distributions for ions bonded to oxygen: results for the lanthanides and actinides and discussion of the *f*-block contraction. *Acta Crystallographica Section B* **74**, 49–62. (10.1107/S2052520617017425)
21. Oikawa K, Kamiyama T, Hashimoto T, Shimojyo Y, Morii Y. 2000 Structural Phase Transition of Orthorhombic $LaCrO_3$ Studied by Neutron Powder Diffraction. *Journal of Solid State Chemistry* **154**, 524–529. (https://doi.org/10.1006/jssc.2000.8873)
22. Lufaso MW, Mugavero SJ, Gemmill WR, Lee Y, Vogt T, zur Loye HC. 2007 Pressure- and temperature-dependent X-ray diffraction studies of $NdCrO_3$. *Journal of Alloys and Compounds* **433**, 91–96. (https://doi.org/10.1016/j.jallcom.2006.06.064)
23. Carpenter MA, Salje EK, Graeme-Barber A. 1998 Spontaneous strain as a determinant of thermodynamic properties for phase transitions in minerals. *European Journal of Mineralogy* **10**, 621–691. (10.1127/ejm/10/4/0621)
24. Dixon CA, Kavanagh CM, Knight KS, Kockelmann W, Morrison FD, Lightfoot P. 2015 Thermal evolution of the crystal structure of the orthorhombic perovskite $LaFeO_3$. *Journal of Solid State Chemistry* **230**, 337–342. (https://doi.org/10.1016/j.jssc.2015.07.019)
25. Capone M, Ridley CJ, Funnell NP, Guthrie M, Bull CL. 2021 Subtle structural changes in $LaFeO_3$ at high pressure. *physica status solidi (b)* **258**, 2000413.
26. Tseggai M, Nordblad P, Tellgren R, Rundlöf H, Andrè G, Bourèe F. 2008 Synthesis, nuclear structure, and magnetic properties of $LaCr_{1-y}Mn_yO_3$ (y=0, 0.1, 0.2, and 0.3). *Journal of Alloys and Compounds* **457**, 532–540. (https://doi.org/10.1016/j.jallcom.2007.03.069)
27. Shukla R, Bera AK, Yusuf SM, Deshpande SK, Tyagi AK, Hermes W, Eul M, Pöttgen R. 2009 Multifunctional nanocrystalline $CeCrO_3$: antiferromagnetic, relaxor, and optical properties. *The Journal of Physical Chemistry C* **113**, 12663–12668.
28. Sau T, Yadav P, Sharma S, Raghunathan R, Manuel P, Petricek V, Deshpande UP, Lalla NP. 2021 High-resolution time of flight neutron diffraction and magnetization studies of spin reorientation and polar transitions in $SmCrO_3$. *Physical Review B* **103**, 144418.
29. Rashad MM, El-Sheikh SM. 2011 Magnetic properties of nano-clusters lanthanum chromite powders doped with samarium and strontium ions synthesized via a novel combustion method. *Materials Research Bulletin* **46**, 469–477.
30. Van Laar B, Elemans JBAA. 1971 On the magnetic structure of $DyCrO_3$. *Journal de Physique* **32**, 301–304.
31. Tripathi M, Chatterji T, Fischer HE, Raghunathan R, Majumder S, Choudhary RJ, Phase DM. 2019 Role of local short-scale correlations in the mechanism of negative magnetization. *Physical Review B* **99**, 014422.
32. Bertaut EF, Mareschal J, De Vries GF. 1967 Etude par diffraction neutronique de la structure magnetique du chromite de terbium. *Journal of Physics and Chemistry of Solids* **28**, 2143–2154.

33. Taheri M, Razavi FS, Yamani Z, Flacau R, Ritter C, Bette S, Kremer RK. 2019 Structural, magnetic, and thermal properties of $Ce_{1-x}Eu_xCrO_3$ orthochromite solid solutions. *Physical Review B* **99**, 054411.
34. Prakash P, Singh R, Mishra SK, Prajapat CL, Kumar A, Das A. 2018 Coupling between Ho and Mn/Cr moments and its influence on the structural and magnetic properties of $HoMn_{1-x}Cr_xO_3$ ($0<x\leq1$) compounds. *Journal of Magnetism and Magnetic Materials* **465**, 70–80.
35. Liu X, Hao L, Liu Y, Ma X, Meng S, Li Y, Gao J, Guo H, Han W, Sun K et al.. 2016 Neutron powder diffraction investigation of magnetic structure and spin reorientation transition of $HoFe_{1-x}Cr_xO_3$ solid solutions. *Journal of Magnetism and Magnetic Materials* **417**, 382–388.
36. Bertaut EF, Mareschal J. 1967 Etude de la structure magnetique des chromites d'erbium et de neodyme par diffraction neutronique. *Solid State Communications* **5**, 93–97.
37. Chakraborty KR, Tyagi AK. 2003 Neutron diffraction study of $La_{1-x}Nd_xCrO_3$ for x= 0.0, 0.05, 0.1, 0.2, and 0.25. *Powder Diffraction* **18**, 285–287.
38. Du Y, Cheng ZX, Wang XL, Dou SX. 2010 Structure, magnetic, and thermal properties of $Nd_{1-x}La_xCrO_3$ ($0 \leq x \leq 1.0$). *Journal of Applied Physics* **108**, 093914.
39. Taguchi H, Matsu-ura Si, Nagao M, Kido H. 1999 Electrical properties of perovskite-type $La(Cr_{1-x}Mn_x)O_{3+\delta}$. *Physica B: Condensed Matter* **270**, 325–331.
40. Qasim I, Blanchard PER, Liu S, Kennedy BJ, Avdeev M. 2014 Impact of Cu Doping on the Structure and Electronic Properties of $LaCr_{1-y}Cu_yO_3$. *Inorganic Chemistry* **53**, 2240–2247.
41. Daniels LM, Weber MC, Lees MR, Guennou M, Kashtiban RJ, Sloan J, Kreisel J, Walton RI. 2013 Structures and Magnetism of the Rare-Earth Orthochromite Perovskite Solid Solution $La_xSm_{1-x}CrO_3$. *Inorganic chemistry* **52**, 12161–12169.
42. Taguchi H, Nagao M, Takeda Y. 1995 Relationship between the electrical properties and crystal structure of $(La_{1-x}Nd_x)CrO_3$ ($0 \leq x \leq 1.0$). *Journal of Solid State Chemistry* **114**, 236–241.
43. Tavizon G, Barreto J, Mata-Ramírez J, Huerta L, Arenas J, de la Mora P, Duran A. 2022 Magnetic and electrical properties by Ca^{2+} doping in $SmCrO_3$ orthochromites. *Journal of Alloys and Compounds* **890**, 161823.
44. Late R, Rai HM, Saxena SK, Kumar R, Sagdeo A, Sagdeo PR. 2016 Probing structural distortions in rare earth chromites using Indian synchrotron radiation source. *Indian Journal of Physics* **90**, 1347–1354.
45. Ramírez JMM, Pessoni HVS, Franco Jr A, Machado FLA. 2017 Synthesis of europium orthochromites ($EuCrO_3$) nanoparticles by a combustion reaction method. *Journal of Alloys and Compounds* **690**, 315–320.
46. Prado-Gonjal J, Schmidt R, Ávila D, Amador U, Morán E. 2012 Structural and physical properties of microwave synthesized orthorhombic perovskite erbium chromite $ErCrO_3$. *Journal of the European Ceramic Society* **32**, 611–618.
47. Yoshii K. 2012 Magnetization reversal in $TmCrO_3$. *Materials Research Bulletin* **47**, 3243–3248.
48. Prado-Gonjal J, Schmidt R, Romero JJ, Ávila D, Amador U, Morán E. 2013 Microwave-assisted synthesis, microstructure, and physical properties of rare-earth chromites. *Inorganic chemistry* **52**, 313–320.
49. Qahtan AAA, Husain S, Somvanshi A, Fatema M, Khan W. 2020 Investigation of alteration in physical properties of dysprosium orthochromite instigated through cobalt doping. *Journal of Alloys and Compounds* **843**, 155637.
50. Shannon RD. 1976 Revised effective ionic radii and systematic studies of interatomic distances in halides and chalcogenides. *Acta Crystallographica Section A* **32**, 751–767. (10.1107/S0567739476001551)
51. Hashimoto T, Tsuzuki N, Kishi A, Takagi K, Tsuda K, Tanaka M, Oikawa K, Kamiyama T, Yoshida K, Tagawa H, Dokiya M. 2000 Analysis of crystal structure and phase transition of $LaCrO_3$ by various diffraction measurements. *Solid State Ionics* **132**, 181–188. (https://doi.org/10.1016/S0167-2738(00)00657-3)
52. Wang D, J. AR. 2011 Octahedral tilts, symmetry-adapted displacive modes and polyhedral volume ratios in perovskite structures.. *Acta Crystallographica B* **67**, 302–314. (https://doi.org/10.1107/S0108768111018313)
53. Rini EG, Gupta MK, Mittal R, Mekki A, Al Saeed MH, Sen S. 2021 Structural change from *Pbnm* to $R\bar{3}c$ phase with varying Fe/Mn content in (1-x)$LaFeO_3$.x$LaMnO_3$ solid solution leading to modifications in octahedral tilt and valence states. *Journal of Alloys and Compounds* **883**, 160761.
54. Johnston KE, Mitchell MR, Blanc F, Lightfoot P, Ashbrook SE. 2013 Structural Study of $La_{1-x}Y_xScO_3$, Combining Neutron Diffraction, Solid-State NMR, and First-Principles DFT Calculations. *The Journal of Physical Chemistry C* **117**, 2252–2265.

55. Cwik M, Lorenz T, Baier J, Müller R, André G, Bourée F, Lichtenberg F, Freimuth A, Schmitz R, Müller-Hartmann E et al.. 2003 Crystal and magnetic structure of $LaTiO_3$: Evidence for nondegenerate t_{2g} orbitals. *Physical Review B* **68**, 060401.
56. Seim H, Fjellvag H, Hauback BC. 1998 Non-stoichiometric $LaVO_3$. II. Powder neutron diffraction study of crystal and magnetic structure for $La_{1-x}VO_3$, $0.00 < x < 0.10$. *Acta chemica scandinavica* **52**, 1301–1306.
57. Dabrowski B, Kolesnik S, Baszczuk A, Chmaissem O, Maxwell T, Mais J. 2005 Structural, transport, and magnetic properties of $RMnO_3$ perovskites (R= La, Pr, Nd, Sm, 153Eu, Dy). *Journal of Solid State Chemistry* **178**, 629–637.
58. Mall AK, Garg N, Verma AK, Errandonea D, Chitnis AV, Srihari V, Gupta R. 2023 Discovery of high-pressure post-perovskite phase in $HoCrO_3$. *Journal of Physics and Chemistry of Solids* **172**, 111078. (https://doi.org/10.1016/j.jpcs.2022.111078)
59. Bhadram VS, Swain D, Dhanya R, Polentarutti M, Sundaresan A, Narayana C. 2014 Effect of pressure on octahedral distortions in $RCrO_3$ (R= Lu, Tb, Gd, Eu, Sm): the role of R-ion size and its implications. *Materials Research Express* **1**, 026111.
60. Ardit M, Cruciani G, Dondi M, Merlini M, Bouvier P. 2010 Elastic properties of perovskite $YCrO_3$ up to 60 GPa. *Physical Review B* **82**, 064109.
61. El Amine Monir M, Dahou FZ. 2020 Structural, thermal, elastic, electronic and magnetic properties of cubic lanthanide based perovskites type oxides $PrXO_3$ (X= V, Cr, Mn, Fe): insights from ab initio study. *SN Applied Sciences* **2**, 1–19.
62. Zhou JS, Alonso JA, Muoñz A, Fernández-Díaz MT, Goodenough JB. 2011 Magnetic Structure of $LaCrO_3$ Perovskite under High Pressure from In Situ Neutron Diffraction. *Physical Review Letters* **106**, 057201. (10.1103/PhysRevLett.106.057201)
63. Jaglinski T, Lakes R. 2007 8. In *Negative Stiffness and Negative Poisson's Ratio in Materials which Undergo a Phase Transformation*, pp. 231–246. John Wiley Sons, Ltd. (https://doi.org/10.1002/9780470512067.ch8)
64. Fujimoto M, Akahama Y, Fukui H, Hirao N, Ohishi Y. 2018 Observation of the negative pressure derivative of the bulk modulus in monoclinic ZrO_2. *AIP Advances* **8**, 015310.
65. Dong L, Stone DS, Lakes RS. 2010 Softening of bulk modulus and negative Poisson ratio in barium titanate ceramic near the Curie point. *Philosophical Magazine Letters* **90**, 23–33. (10.1080/09500830903344907)
66. Bull CL, Ridley CJ, Knight KS, Funnell NP, Gibbs AS. 2021 Comprehensive determination of the high-pressure structural behaviour of $BaTiO_3$. *Matererials Advances* **2**, 6094–6103. (10.1039/D1MA00651G)
67. Ghose S. 1985 Microscopic to Macroscopic. *Min. Soc. Am.* pp. 127–163.
68. Baur WH. 1974 The geometry of polyhedral distortions. Predictive relationships for the phosphate group. *Acta Crystallographica Section B* **30**, 1195–1215. (10.1107/S0567740874004560)
69. Brown ID, Altermatt D. 1985 Bond-valence parameters obtained from a systematic analysis of the Inorganic Crystal Structure Database. *Acta Crystallographica Section B* **41**, 244–247. (10.1107/S0108768185002063)
70. Brese NE, O'Keeffe M. 1991 Bond-valence parameters for solids. *Acta Crystallographica Section B* **47**, 192–197. (10.1107/S0108768190011041)
71. Hashimoto T, Matsushita N, Murakami Y, Kojima N, Yoshida K, Tagawa H, Dokiya M, Kikegawa T. 1998 Pressure-induced structural phase transition of $LaCrO_3$. *Solid state communications* **108**, 691–694.
72. Shibasaki T, Furuya T, Kuwahara J, Takahashi Y, Takahashi H, Hashimoto T. 2005 Exploration of high pressure phase in $LaGaO_3$ and $LaCrO_3$. *Journal of thermal analysis and calorimetry* **81**, 575–581.
73. Weber MC, Kreisel J, Thomas PA, Newton M, Sardar K, Walton RI. 2012 Phonon Raman scattering of $RCrO_3$ perovskites ($R = $ Y, La, Pr, Sm, Gd, Dy, Ho, Yb, Lu). *Physical Review B* **85**, 054303. (10.1103/PhysRevB.85.054303)
74. Iliev MN, Litvinchuk AP, Hadjiev VG, Wang YQ, Cmaidalka J, Meng RL, Sun YY, Kolev N, Abrashev MV. 2006 Raman spectroscopy of low-temperature $(Pnma)$ and high-temperature $(R\bar{3}c)$ phases of $LaCrO_3$. *Physical Review B* **74**, 214301. (10.1103/PhysRevB.74.214301)
75. Court CJ, Cole JM. 2020 Magnetic and superconducting phase diagrams and transition temperatures predicted using text mining and machine learning. *npj Computational Materials* **6**, 1–9.
76. Bull CL, Ridley CJ, Funnell NP. 2019 Structural and Magnetic Behaviour of $PrCrO_3$ at High Pressure. *STFC ISIS Neutron and Muon Source*. (https://doi.org/10.5286/ISIS.E.RB1910180)

77. Ridley CJ, da Silva Gonzalez I. 2019 Investigating the magnetic structure of the solid solution $PrCr_{(1-x)}Mn_xO_3$. *STFC ISIS Neutron and Muon Source*. (https://doi.org/10.5286/ISIS.E.RB1910412-1)
78. Ridley CJ, Smith RI. 2018 Ambient conditions neutron diffraction study of $PrCrO_3$. *STFC ISIS Neutron and Muon Source*. (https://doi.org/10.5286/ISIS.E.RB1890109-1)